

# ASSESSMENT OF SHOULDER-BED, INVASION, AND LAMINATION EFFECTS ON BOREHOLE SONIC LOGS: A NUMERICAL SENSITIVITY STUDY

A. Peyret and C. Torres-Verdín, The University of Texas at Austin

Copyright 2006, held jointly by the Society of Petrophysicists and Well Log Analysts (SPWLA) and the submitting authors.

This paper was prepared for presentation at the SPWLA 47<sup>th</sup> Annual Logging Symposium held in Veracruz, Mexico, June 4-7, 2006.

## ABSTRACT

We quantify the relative effects of shoulder beds, layer thickness, invasion, and sand-shale laminations on monopole and dipole borehole sonic logs. This is accomplished through numerical simulation of sonic waveforms that includes all of the propagation modes within the 1-10 KHz range. Numerical simulations assume infinitesimal monopole and dipole sources as well as an array of infinitesimal receivers deployed in close similarity with one commercially available wireline sonic tool. Propagation modes and their velocities are assessed via slowness-time-coherence processing of the simulated waveforms.

For the case of shoulder-bed and layer-thickness effects, we consider soft and hard formations bounded by shale layers. The thickness of the formation is changed to consider cases where transmitter and receivers are completely included in the bed and partially distributed across different beds. Simulations indicate that shoulder- and bed-thickness effects can account for up to 33% variations in the P-wave velocities measured with a monopole source and 31% in the measured S-wave velocities measured with a dipole source compared to those measured across infinitely thick beds.

We reproduce the sonic response of sand-shale laminated formations by including thin shale layers within pay sands. The thickness of shale layers is varied to consider the effect of proportion of sand and shale on the measurements. Simulations indicate that shale laminations can account for up to 16.4% variations in the P-velocities measured with a monopole source and up to 3.6% variations in the S-velocities measured with a dipole source with respect to those of effective lamination velocities.

Effects of invasion are simulated for the case of water-base mud invading oil-bearing formations. Our simulations indicate that P-wave sonic logs can undergo

up to 13% variations due to invasion under realistic assumptions of petrophysical and elastic properties of soft and hard formations.

## INTRODUCTION

Over the years, sonic tools have been widely used to assess mechanical and petrophysical properties of rock formations penetrated by a well. Sonic measurements are an essential component of most well-log interpretation procedures.

The length of the transmitter-sensor array normally used to acquire sonic measurements limits the vertical resolution of the interpreted elastic properties, thus producing results that respond to averaged properties when the thickness of the beds is shorter than the length of the array. As in the case of several other wireline logging measurements, conventional procedures used to estimate elastic properties of rock formations from array sonic measurements can be deleteriously affected by unaccounted presence of shoulder beds, thin beds, and sand-shale laminations. In addition, the process of mud-filtrate invasion can have adverse effects on sonic logs, thereby biasing the measurement of in-situ formation properties and making log interpretation more difficult.

When Kokesch and Blizzard (1959) published their fundamental paper about "Geometrical Factors in Sonic Logging" almost half a century ago, they assumed a compensated sonic tool consisting of one transmitter and one or two receivers. Their work was the first formal attempt to quantify the effect of shoulder beds and thin beds on time-of-arrival measurements. Since then, significant advances have been made in the acquisition and processing of sonic waveforms for the measurement of elastic properties of rock formations. Recent publications such as that of Schön *et al.* (2005) provide very detailed calculations about wave propagation properties in heterogeneous and anisotropic rock formations and their impact on array sonic measurements, but fail to take into consideration environmental, petrophysical, and geometrical effects that could bias the estimation of elastic properties.

Therefore, a study is in order to assess the influence of the same geometrical factors described by Kokesh and Blizard (1959) on modern borehole array sonic measurements. The work described in this paper makes use of numerical simulation to model the complete borehole sonic waveforms acquired with monopole and dipole transmitters. Our objective is to quantify the effects of shoulder beds, thin beds, sand-shale laminations, and mud-filtrate invasion on the estimation of P- and S-wave velocities of rock formations performed with standard waveform processing methods.

### SYNTHETIC ROCK MODELS

We consider four basic synthetic models for the numerical sensitivity study presented in this paper. Simulation of borehole sonic logs is performed assuming specific source-receiver configurations available from the new Schlumberger array sonic tool introduced by Pistre *et al.* (2005) and schematically described in Fig. 1. Tables 1 through 3 summarize the elastic and geometrical parameters assumed in the various synthetic formation models considered in this paper.

Fig. 2 shows Model 1, intended for the study of shoulder-bed effects. It consists of two horizontal layers with different elastic properties. The contrast in P- and S-wave velocities,  $V_P$  and  $V_S$  respectively, as well as in density,  $\rho$ , are modified in order to assess their influence on the simulated logs. Thickness of the layers is chosen greater than the length of the tool in order to simulate sonic measurements acquired along the complete vertical transition zone between the two layers.

As illustrated in Fig. 3, Model 2 consists of three layers, including two shale beds thicker than the length of the transmitter-receiver array, and one inner sand bed thinner than the length of the receiver array. We examine four specific variations of this model and consider a range of contrasts of elastic properties and center-bed thicknesses.

Model 3, described in Fig. 4, is a variation of Model 2, where the center bed has been replaced with sand-shale laminations of thicknesses equal or smaller than the distance between adjacent tool receivers. The first five sub models (a,b,c,e,f) consider various proportions of soft and hard layers (50%/50%, 37.5%/62.5% and 62.5%/37.5%, 25%/75%, 75%/25%), whereas the last sub model (d) considers a smaller contrast in elastic properties than the first one while assuming the same proportion (50%/50%) of soft and hard layers.

The last model considered in this paper, shown in Fig. 5, is a variation of Model 2 designed to appraise the effect of mud-filtrate invasion on sonic logs. The process of mud-filtrate invasion is simulated assuming fresh water-base mud. Biot-Gassmann's equations (Smith *et al.*, 2003) are used to quantify variations of velocity due to variations of fluid saturation and to update the values of  $V_P$ ,  $V_S$ , and density, with respect to those of the uninvaded rock formation. Moreover, in order to keep the invasion model as simple as possible, we assume a piston-like invasion front. The radial length of invasion for each layer is chosen proportional to  $\sqrt{2/\phi}$ , where  $\phi$  is the assumed value of porosity for the invaded layer.

All synthetic formation models considered in this paper assume a borehole radius equal to 10.16 cm. The borehole is filled with fresh water ( $V_P=1,500\text{m/s}$ ,  $V_S=0$ ,  $\rho=1,000\text{kg/m}^3$ ).

### NUMERICAL SIMULATION AND WAVEFORM PROCESSING

The numerical algorithm used to simulate sonic waveforms is based on the finite-difference approximation of the stress-velocity hyperbolic partial differential equation of wave propagation in elastic transverse-isotropic axial-symmetric media (Xu *et al.*, 2005). We make use of a staggered finite-difference approach for velocity and stress to discretize the wave propagation equation and the elastic properties in a two-dimensional cylindrical coordinate frame. Time-domain solutions of wave propagation are obtained with a second-order time marching scheme coupled with either second- or fourth-order discretization in space. In addition, we enforce absorbing boundary conditions to effectively truncate the domain of spatial discretization in the radial and vertical directions. Simulations of sonic waveforms are performed for cases of infinitesimal monopole, dipole, and quadrupole transmitters for a range of source wavelets and frequency spectra in the 1-15 kHz range. Extensive benchmarking and testing of the numerical simulation algorithm indicates that the simulated waveforms have an accuracy of better than 2%.

As noted earlier, Figure 1 describes the array sonic tool assumed in the numerical simulation of sonic waveforms. The tool includes an array receiver section composed of 13 receiver stations separated at a uniform distance of 0.5ft. Sources consist of three monopole and two dipole transmitters. Monopole sources are located at distances of -7ft to -1ft (referred as Upper Monopole), 1ft to 7ft (Lower Monopole) and 11ft to 17ft (Far Monopole) from the receiver array,

respectively. Dipole transmitters are located at distances of 9ft to 15ft and 10ft to 16ft from the sensor array, respectively.

Figures 6 and 7 show examples of numerically simulated sonic waveforms for the case of dipole and monopole sources included in the wireline tool described in Fig. 1. In both cases, we assumed a zero-phase Ricker wavelet (centered at a frequency of 8 KHz for the monopole source and 2 kHz for the dipole source) to simulate the waveforms.

Simulated sonic waveforms are subsequently subject to slowness-time-coherence (STC) processing to detect modes of propagation and to assess their corresponding velocities. Figures 8 and 9 are STC plots associated with the sonic waveforms shown in Figs. 6 and 7, respectively. The calculated velocities correspond to points of maximum coherence on the STC plot.

Because of the finite length of the tool, it is impossible to precisely match depth in the formation with the position of the tool. In this paper, we use the center point of the receiver array to designate the depth of the sonic measurement with respect to the probed formation. Therefore, when we state that “the tool is located 30.48cm below the bed boundary,” we mean that “the mid-point of the array of receivers is located 30.48cm below the bed boundary.”

## SIMULATION RESULTS

### *Shoulder-Bed Effects*

Figs. 10 through 13 show the simulated logs for Model 1 (described in Fig. 2). The simulations include two-bed interface transitions for a variety of contrasts in elastic properties and types of sources used to acquire the sonic measurements. Results show that the calculated P-wave velocities are more affected by the vertical transition than the calculated S-wave velocities when compared to the original model. Table 4 describes an example of calculated P- and S-wave velocities from waveform simulation and subsequent STC processing (Model 1a for the case of the far monopole source). In the presence of a high velocity contrast (Model 1a), the difference between the calculated P-wave velocities and the original input velocities varies from -3.7% to +3.0% when using the far monopole. On the other hand, as shown in Fig. 10, differences between calculated and original S-wave velocities vary between -8.8% and -4.4% for the far dipole source. The order of magnitude of the difference between calculated and original velocities remains the same when the contrast of velocity is slightly decreased, as indicated by the simulation results for Model 1b, plotted in Fig. 11.

Similarly, Model 1c shows that the calculated P-wave velocities are, at the transition zone, under-estimated with respect to those of the original model (up to -20.2% with the far monopole source) before the bed boundary and over-estimated (up to 10.9% with the same sonic source) after the bed boundary. In the presence of a small velocity contrast in a soft formation (as the one included in Model 1d), the calculated sonic logs still tend to overestimate  $V_p$  after the bed boundary more than it underestimates it before the bed boundary. For the case of the far monopole source, calculated velocities vary between -5.3% and +8.9% of the original values of  $V_p$ . S-wave sonic logs simulated with the far dipole source vary between -12.8% and +6.2% of the original formation velocities. Figs. 12 and 13 show the simulated logs for Models 1c and 1d, respectively.

### *Thin-Bed Effects*

Simulation results for Model 2 (shown in Fig. 3) are described in Figs. 14 through 17. The objective of this simulation is to assess the effect of bed thickness for a range of contrasts of elastic properties between the center and shoulder beds. In particular, we examine the effect of bed thickness smaller than both the transmitter-receiver distance and the length of the array of receivers. Results show that the calculated P- and S-velocities are often over-estimated when the center bed is softer than the shoulder beds, leading up to 18% of variations of the calculated  $V_p$  log with respect to the effective averaged model values when the monopole source is used for waveform acquisition (Model 2a, as shown in Fig. 14). The maximum difference in the calculated velocities with respect to effective averaged model ones lies between -4.8% and +13.6% for the case of the far monopole source ( $V_p$ ), and between -7.7% and -3.25% for the case of the far dipole source ( $V_s$ ), so that calculated S-wave velocities acquired using the dipole source are closer to those of the original model than the calculated P-wave velocities acquired using the monopole source. This observation applies to all simulation examples associated with Model 2. The simulations also indicate that, in general, when using with the monopole source, the thicker the layer the larger the difference between calculated and original model velocities when the contrast of velocity is high. However, the difference between calculated and original P-velocity values stays the same when the velocity contrast between center bed and shoulders is low. We also note that although the S-velocities computed using the dipole source lie far (~5%) from the theoretical values, the computed  $V_s$ -curves look parallel to the theoretical ones, so that the error in the sand section can be greatly reduced by estimating the error in the adjacent shale.

**Effect of Sand-Shale Laminations**

Figs. 18 through 23 describe the simulated P- and S-wave velocity logs associated with Model 3 (shown in Fig. 4). The objective of the simulations is to quantify the effect of thin shale laminations included in an otherwise clean sand bed. We compare the calculated P- and S-wave velocities to the effective velocities of the lamination derived from White and Angona's (1954) equations.

The simulated sonic logs for Model 3 can be appraised in terms of the effective elastic properties of laminated sands discussed by White and Angona (1954). The formula used for computing the theoretical averaged velocity in a laminated section, as given by White and Angona, is:

$$V = \frac{1}{\sqrt{\left[ \frac{1-C_{SH}}{\rho_{SD} V_{SD}^2} + \frac{C_{SH}}{\rho_{SH} V_{SH}^2} \right] [(1-C_{SH})\rho_{SD} + C_{SH}\rho_{SH}]}}$$

where:

- V is the averaged velocity (P or S) in the laminated section,
- V<sub>SD</sub> is the velocity (P or S, same as V) of the sand laminations,
- V<sub>SH</sub> is the velocity (P or S, same as V) of the shale laminations,
- C<sub>SH</sub> is the fraction of shale in the laminations, and
- ρ<sub>SD</sub> and ρ<sub>SH</sub> are the densities of the sand and the shale laminations respectively.

We modify the above equation to take into account the real volume of shale within the array of receivers (that should be longer than the thickness of the laminated zone for this formula to be valid):

$$\frac{V_{min}}{L} = \frac{1}{\sqrt{\left[ \frac{TC_s}{\rho_{SD} V_{SD}^2} + \frac{L-TC_s}{\rho_{SH} V_{SH}^2} \right] [TC_s\rho_{SD} + (L-TC_s)\rho_{SH}]}}$$

where:

- L is the length of the array of receivers,
- T is the thickness of the laminated zone (T<L),
- C<sub>s</sub> is the fraction of sand in the laminations,
- The laminations are included in a (sand free) shale section,
- The laminated and adjacent shales have the same elastic properties, and
- No assumption is made about the internal distribution of the sand and shale layers.

This equation is the minimum theoretical averaged velocity that may be reached when the laminations are completely included between the first and last receivers. For the comparisons, we use an effective velocity, and we plot it with black dashed lines in Figs. 18 through 23, that we compute by summing the thicknesses of sand layers between the first and last receivers of the

tool, normalized by the length of the receiver array, and using this value as the effective volume of sand.

If we assume that the velocity measured by a sonic tool in a formation with sand-shale laminations is the lowest of our simulated values (simulated when the sensor array is positioned at the mid point of the laminated section), then we obtain a very good fit between the calculated velocities (as functions of the proportion of shale and sand in Model 3) and the theoretical averaged velocities (as given by the last equation) on the whole interval of sand-shale proportions that we consider (Figs. 24 and 25). We also obtain minimal values that match the effective velocities with an error less than ±1.3% for the monopole source and less than -5.9±1.13% for the dipole source.

Simulated sonic logs for the first five models (3a, 3b, 3c, 3e and 3f) of laminated soft/hard formations indicate that the proportion of soft (sand) and hard (shale) formation components in the lamination has no appreciable effect on V<sub>p</sub> when compared to the effective velocity of the lamination zone (including the bed shoulders). The calculated P-wave velocity log is often overestimated, as it remains between -1.9% (±1.4%) and +5.7% (±7.4%) with respect to the effective velocity of the lamination calculated with the far monopole source. However, the calculated S-wave velocity log is often underestimated, as it stays between -6.2% (±0.9%) and -3.9% (±0.44%) when calculated with the far dipole source.

**Effect of Fresh-Water Mud-Filtrate Invasion**

Figs. 26 and 27 describe the simulated sonic logs for the model of a single invaded bed (Model 4, shown in Fig. 5). The objective of the simulations is to quantify the variation of measured velocities in the invaded state with respect to those of the uninvaded rock formation.

When the oil-bearing formation is invaded with fresh water-base mud, the thickness of the invaded layer does not have an appreciable effect in the calculated velocities for the case of a monopole source, nor does it affect the calculated shear-wave velocities for the case of the dipole source. Differences in the calculated P-wave velocity logs with respect to the original uninvaded model velocities for the case of a monopole source remain between -1.8% and +12.1% (-0.9% to +12.1% for the case of a thick layer and -1.8% to +7.1% for the case of a thin layer). Calculated shear-wave velocities vary between -0.8% and +1.7% of the original uninvaded bed velocities for the case of the dipole source. The smallest difference between the calculated velocities and the original uninvaded bed velocities is associated with the S-wave velocity across

the thinner layer when using a dipole source (-0.43% to +0.0%, Fig. 27).

## DISCUSSION

Numerical simulations undertaken in this paper suggest that both the length of the receiver array and the contrast of elastic properties condition the relative difference between calculated and original model velocities. In some cases, the averaging of elastic properties enforced by the receiver array leads to substantial differences between calculated and original velocities regardless of the type of source used to generate the sonic waveforms. Although not shown in this paper, such differences can be larger than relative variations in P- and S-wave velocities due to variations of fluid saturation, porosity, shale content, and even degree of anisotropy, thereby masking important petrophysical effects on the STC-processed velocities. It is anticipated that the use of sonic waveforms acquired with a sub-array of receivers will decrease the averaging length and, therefore, improve the sensitivity of the measurements to variations of petrophysical properties of thin beds or across bed interface transitions (possibly at the expense of the deleterious influence of measurement noise). A possible solution to this problem is the use of frequency-dependent adaptive sub-array selection and waveform processing.

## CONCLUSIONS

Velocities calculated with dipole sources are closer to original model values in thin beds (thinner than the length of the receiver array), but velocities calculated with a monopole sonic source are closer to original model velocities in thick beds. Simulated and STC-processed waveforms for dipole sources often yield calculated velocities lower than the original model velocities, whereas there is no general rule for monopole sources. For cases of high contrast in formation velocities between thick beds, calculated P-wave velocities differ from the original model velocities by ~33% at most (~10% with a low contrast in velocities or for the case of thin beds), whereas calculated S-wave velocities differ by ~31% at most.

When compared to original velocities of uninvaded rock formations, the effect of mud-filtrate invasion on calculated sonic logs is smaller than the effect of bed thickness, especially for the case of beds thinner than the length of the sensor array. Percent differences between calculated and effective sand velocities across sand-shale laminated formations are similar for monopole and dipole acquisitions.

In the presence of laminations or for the case of sand-bed inclusions in a shale section, calculated S-wave velocities can differ by -7.7 to -1.3% from the original model velocities for the case of a dipole. Invasion effects account for up to +13% differences between calculated and original P-velocities for the case of a monopole source, and for up to +2.5% difference between calculated and original S-wave velocities for the case of a dipole source.

Another important observation concerns the assessment of bed thickness for the cases of thin-bed and lamination effects. If the array of receivers is longer than the thickness of the thin-bed (or laminated section), the theoretical averaged velocity should exhibit a plateau when the receivers cover the bed completely. The length of this plateau is equal to the difference between the length of the receiver array and the bed thickness, thereby allowing an estimation of the bed thickness by processing the raw data with various numbers of receivers. The plateau then disappears when length of the receiver array is equal to the thickness of the bed, and the averaged velocity obtained in this case is equal to the one predicted using the original formula by White and Angona.

The simulations described in this paper considered only one value of peak frequency for the assumed Ricker source wavelet for each source (8 kHz for the monopole source and 2 kHz for the dipole source). Work still remains to quantify possible frequency-dependent effects on calculated sonic logs due to shoulder beds, thin beds, laminations, and invasion. Such quantification merits the use of wide-band frequency dispersion analysis for the calculation of sonic logs. Similarly, work remains to assess the influence of the same environmental effects on the detection and evaluation of anisotropic modes of wave propagation contained in simulated sonic waveforms.

## ACKNOWLEDGMENTS

Funding for the work reported in this paper was provided by UT Austin's Research Consortium on Formation Evaluation, jointly sponsored by Aramco, Baker Atlas, BP, British Gas, ConocoPhillips, Chevron, ENI E&P, ExxonMobil, Halliburton Energy Services, Marathon, Mexican Institute for Petroleum, Norsk-Hydro, Occidental Petroleum Corporation, Petrobras, Schlumberger, Shell International E&P, Statoil, Total, and Weatherford.

## REFERENCES

- Kokesh, F. P., and Blizard, R. B., 1959, Geometrical factors in sonic logging, *Geophysics*, v. 24, n. 1, 64-76.
- Pistre, V., Kinoshita, T., Endo, T., Schilling, K., Pabon, J., Sinha, B., Plona, T., Ikegami, T., and Johnson, D., 2005, A modular wireline sonic tool for measurements of 3D (azimuthal, radial, and axial) formation acoustic properties: SPWLA 46<sup>th</sup> Annual Logging Symposium, Expanded Abstracts, New Orleans, LA.
- Schön, J., Georgi, D., and Tang, X., 2005, Elastic wave anisotropy and shale distribution: SPWLA 46<sup>th</sup> annual Logging Symposium, Expanded Abstracts, New Orleans, LA.
- Smith, T.M., Sondergeld, C.H., and Rai, C.S., 2003, Gassmann fluid substitutions: a tutorial, *Geophysics*, v. 68, n. 2, 430-440.
- White, J.E., Angona, F.A., 1954, Elastic wave velocities in laminated media, *Journal of the Acoustical Society of America*, v. 27, n. 2, 310-317.
- Xu, Y., Hou, J., and Torres-Verdín, C., 2005, Fast and efficient 2.5D time-domain simulation of multi-pole sonic logs: elastic and poro-elastic transverse isotropic formulations, Presented at the Annual Meeting of UT Austin's Research Consortium on Formation Evaluation.

## ABOUT THE AUTHORS

**Aymeric Peyret** received an engineering degree from the École Centrale de Lille, France, and is currently a Graduate Research Assistant and a Master of Science candidate in Petroleum Engineering at the University of Texas at Austin. His professional interests include sonic-log interpretation, numerical simulation, signal processing, and formation evaluation. Aymeric's Master's thesis focuses on the quantitative analysis of waveform sonic measurements acquired in axial-symmetric transverse-isotropic media.

**Carlos Torres-Verdín** received a PhD in Engineering Geoscience from the University of California, Berkeley, in 1991. During 1991-1997 he held the position of

Research Scientist with Schlumberger-Doll Research. From 1997-1999, he was Reservoir Specialist and Technology Champion with YPF (Buenos Aires, Argentina). Since 1999, he has been with the Department of Petroleum and Geosystems Engineering of The University of Texas at Austin, where he currently holds the position of Associate Professor. He conducts research on borehole geophysics, formation evaluation, and integrated reservoir characterization. Torres-Verdín has served as Guest Editor for *Radio Science*, and is currently a member of the Editorial Board of the *Journal of Electromagnetic Waves and Applications*, and an associate editor for *Petrophysics* (SPWLA) and the *SPE Journal*.

| Model | $V_{P1}$ (m/s) | $V_{S1}$ (m/s) | $\rho_1$ (kg/m <sup>3</sup> ) | $V_{P2}$ (m/s) | $V_{S2}$ (m/s) | $\rho_2$ (kg/m <sup>3</sup> ) | Total time |
|-------|----------------|----------------|-------------------------------|----------------|----------------|-------------------------------|------------|
| 1a    | 2,850          | 1,275          | 2,480                         | 2,000          | 1,204          | 2,050                         | 6 ms       |
| 1b    | 2,650          | 1,150          | 2,350                         | 2,000          | 1,204          | 2,050                         | 6 ms       |
| 1c    | 2,350          | 966            | 2,150                         | 2,000          | 1,204          | 2,050                         | 6 ms       |
| 1d    | 2,850          | 1,275          | 2,480                         | 2,350          | 966            | 2,150                         | 8 ms       |
| 2a    | 2,850          | 1,275          | 2,480                         | 2,000          | 1,204          | 2,050                         | 6 ms       |
| 2b    | 2,850          | 1,275          | 2,480                         | 2,663          | 1,191          | 2,317                         | 6 ms       |
| 2c    | 2,850          | 1,275          | 2,480                         | 2,000          | 1,204          | 2,050                         | 6 ms       |
| 2d    | 2,850          | 1,275          | 2,480                         | 2,663          | 1,191          | 2,317                         | 6 ms       |
| 3a    | 2,850          | 1,275          | 2,480                         | 2,000          | 1,204          | 2,050                         | 6 ms       |
| 3b    | 2,850          | 1,275          | 2,480                         | 2,000          | 1,204          | 2,050                         | 6 ms       |
| 3c    | 2,850          | 1,275          | 2,480                         | 2,000          | 1,204          | 2,050                         | 6 ms       |
| 3d    | 2,850          | 1,275          | 2,480                         | 2,663          | 1,191          | 2,317                         | 6 ms       |
| 3e    | 2,850          | 1,275          | 2,480                         | 2,000          | 1,204          | 2,050                         | 6 ms       |
| 3f    | 2,850          | 1,275          | 2,480                         | 2,000          | 1,204          | 2,050                         | 6 ms       |
| 4a    | 2,850          | 1,275          | 2,480                         | 2,000          | 1,204          | 2,050                         | 6 ms       |
| 4b    | 2,850          | 1,275          | 2,480                         | 2,000          | 1,204          | 2,050                         | 6 ms       |

**Table 1:** *P- and S-wave velocities and densities assumed for the various example models considered in this paper.*

| Model        | 1a, 1b, 1c, 1d             | 2a, 2b, 3a, 3b, 3c, 3d, e, 3f, 4a | 2c, 2d, 4b       |
|--------------|----------------------------|-----------------------------------|------------------|
| First Layer  | 9.14m (30 ft)              | 5.26m (17.25 ft)                  | 5.26m (17.25 ft) |
| Second Layer | 18.29m (60 ft)             | 1.52m (5 ft)                      | 0.76m (2.5 ft)   |
| Third Layer  | Only two layers in Model 1 | 5.26m (17.25 ft)                  | 7.54m (24.75 ft) |

**Table 2:** *Thicknesses of the horizontal layers assumed for the various example models considered in this paper.*

| Model Property           | 3a       | 3b       | 3c       | 3d       | 3e      | 3f      |
|--------------------------|----------|----------|----------|----------|---------|---------|
| Thickness of soft layers | 10.16 cm | 12.70 cm | 7.62cm   | 10.16 cm | 5.08cm  | 15.24cm |
| Thickness of hard layers | 10.16 cm | 7.62cm   | 12.70 cm | 10.16 cm | 15.24cm | 5.08cm  |

**Table 3:** *Thicknesses of the sand-shale laminations assumed for Model 3*

|                      |       |       |       |       |       |       |       |       |       |       |       |      |      |      |
|----------------------|-------|-------|-------|-------|-------|-------|-------|-------|-------|-------|-------|------|------|------|
| <b>d (m)</b>         | -1.61 | -1.45 | -1.30 | -1.15 | -1.00 | -0.84 | -0.69 | -0.54 | -0.39 | -0.23 | -0.08 | 0.07 | 0.22 | 0.38 |
| <b>V<sub>P</sub></b> | 2822  | 2822  | 2822  | 2822  | 2822  | 2796  | 2822  | 2796  | 2796  | 2771  | 2746  | 2059 | 2032 | 2032 |
| <b>V<sub>S</sub></b> | 1224  | 1224  | 1224  | 1224  | 1224  | 1219  | 1210  | 1200  | 1191  | 1177  | 1168  | 1155 | 1146 | 1133 |
| <b>d (m)</b>         | 0.53  | 0.68  | 0.83  | 0.98  | 1.14  | 1.29  | 1.44  | 1.59  | 1.75  | 1.90  | 2.05  | 2.20 | 2.36 | 2.51 |
| <b>V<sub>P</sub></b> | 2019  | 2005  | 2005  | 1992  | 1992  | 1992  | 1992  | 1992  | 1992  | 1992  | 1992  | 1992 | 1992 | 1992 |
| <b>V<sub>S</sub></b> | 1125  | 1116  | 1108  | 1121  | 1121  | 1121  | 1121  | 1121  | 1121  | 1121  | 1121  | 1121 | 1121 | 1121 |

**Table 4:** *Velocities (in m/s) calculated from STC processing of sonic waveforms simulated for Model 1a assuming a far-monopole source for  $V_P$  and a far dipole source for  $V_S$ . The variable  $d$  is the distance (in meters) between the last receiver and the bed boundary. The velocities  $V_P$  and  $V_S$  were calculated from the local maxima STC plots.*

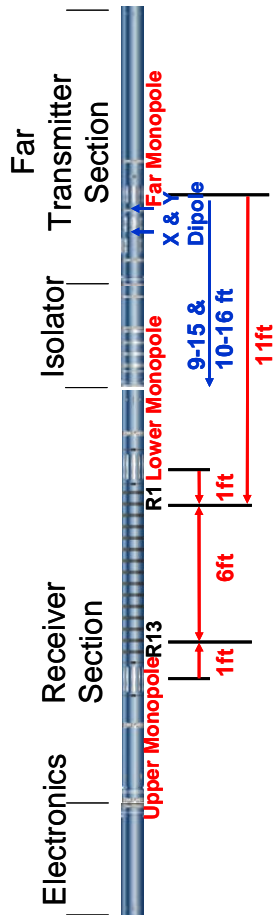


**Fig. 1:** Description of the wireline sonic tool assumed in the numerical simulations reported in this paper (adapted from the paper by Pistre et al., 2005)

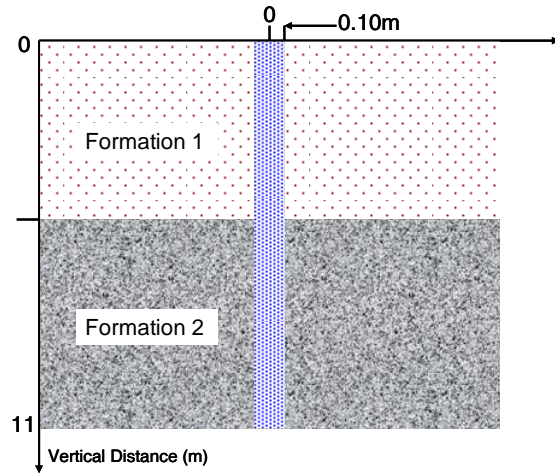


**Fig. 2:** Model 1, consisting of two horizontal layers with varying contrasts of elastic properties.

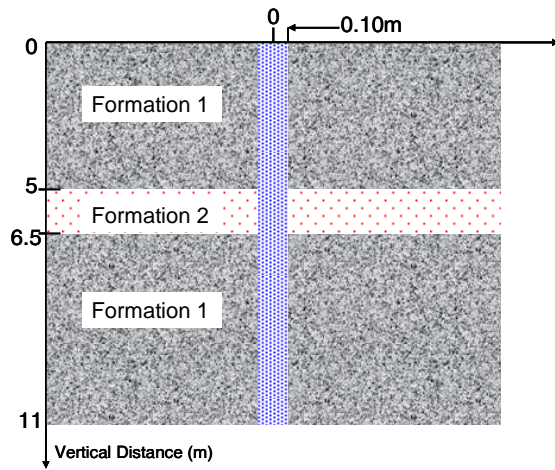


**Fig. 3:** Model 2, consisting of one horizontal bed of variable thicknesses located between two horizontal shouldering layers. The model includes variable contrasts of elastic properties and variable bed thicknesses.

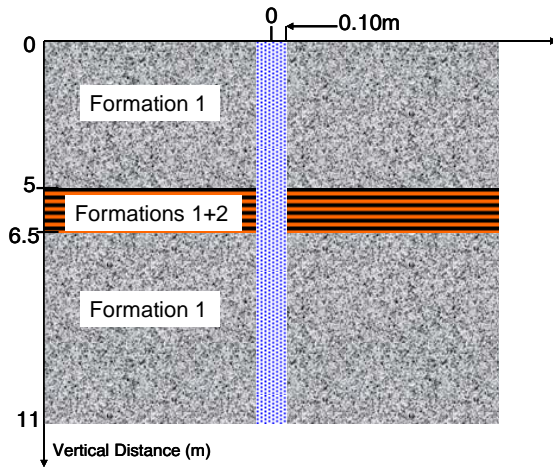


**Fig. 4:** Model 3, consisting of a center horizontal bed with sand-shale laminations of varying sand-shale proportions and varying contrasts of elastic properties.

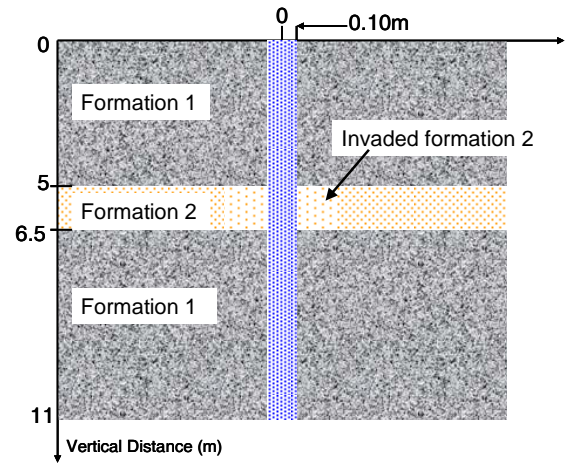


**Fig. 5:** Model 4, consisting of two special cases of Model 2 to consider presence of fresh-water mud-filtrate invasion.

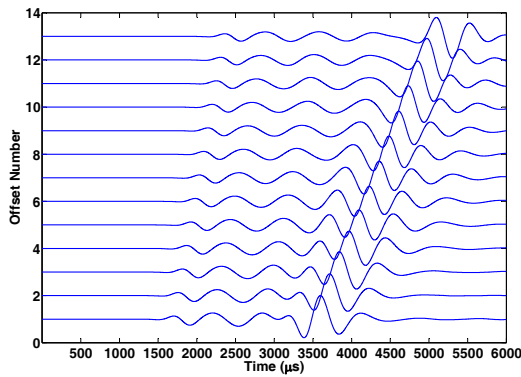


**Fig. 6:** Example of sonic waveforms simulated with the far dipole transmitter of the tool shown in Fig. 2 for the case of Model 1c.

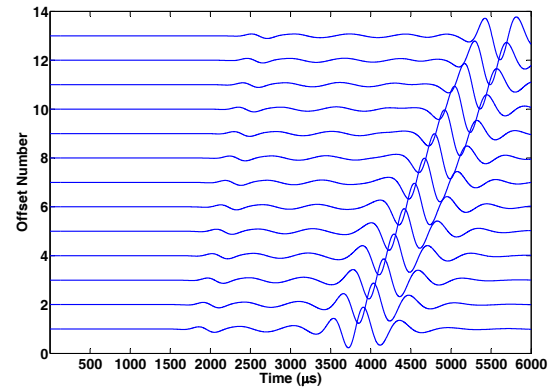


**Fig. 7:** Example of sonic waveforms simulated with the far-monopole transmitter of the tool shown in Fig. 1 for the case of Model 2b.

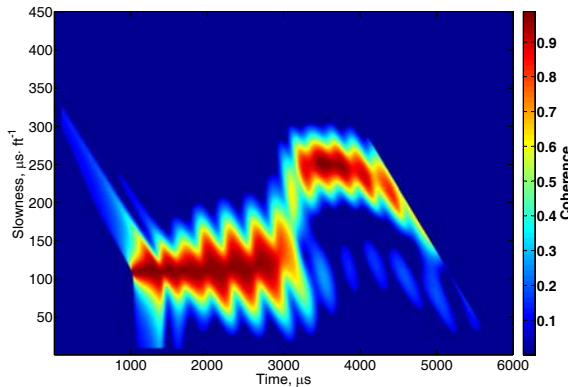


**Fig. 8:** Slowness-Time-Coherence plot for sonic waveforms (Fig. 6) simulated with a dipole source for the case of Model 1c.

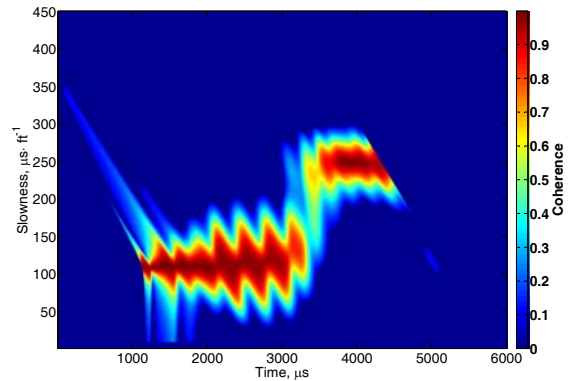


**Fig. 9:** Slowness-Time-Coherence plot for sonic waveforms (Fig. 7) simulated for a far monopole source for the case of Model 2b.

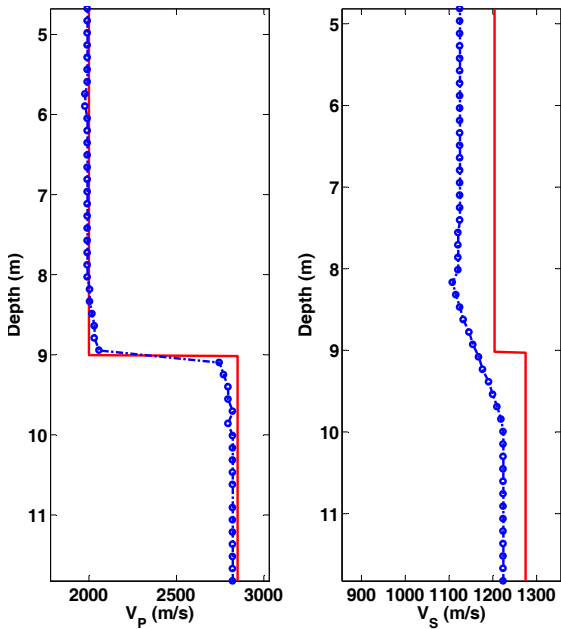


**Fig. 10:** Logs of  $V_P$  (monopole source) and  $V_S$  (dipole source) for Model 1a. Continuous and dotted lines identify input (model) and numerically calculated velocities, respectively.

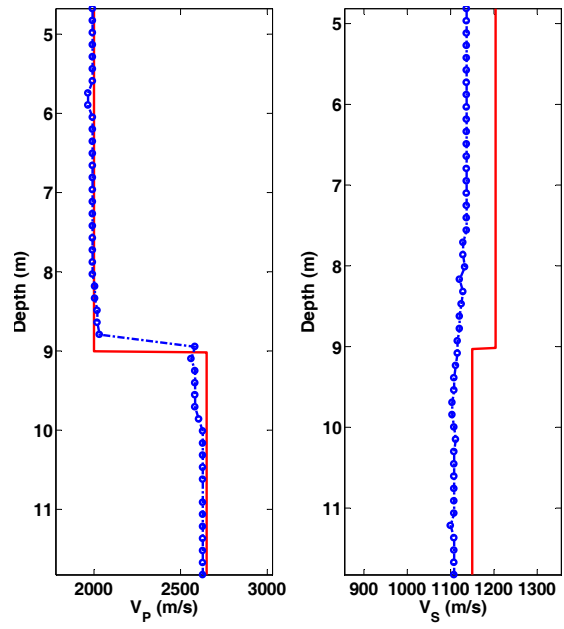


**Fig. 11:** Logs of  $V_P$  (monopole source) and  $V_S$  (dipole source) for Model 1b. Continuous and dotted lines identify input (model) and numerically calculated velocities, respectively.

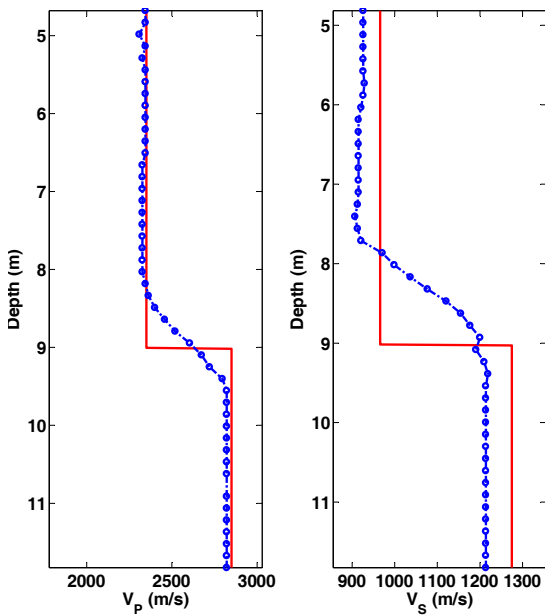


**Fig. 12:** Logs of  $V_P$  (monopole source) and  $V_S$  (dipole source) for Model 1c. Continuous and dotted lines identify input (model) and numerically calculated velocities, respectively.

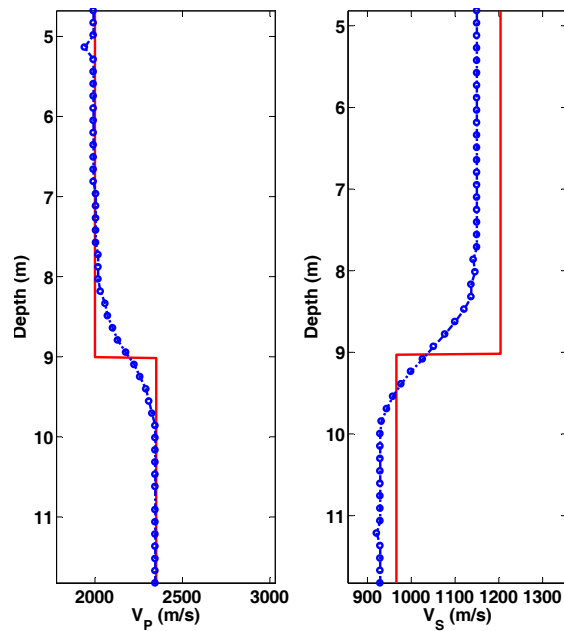


**Fig. 13:** Logs of  $V_P$  (monopole source) and  $V_S$  (dipole source) for Model 1d. Continuous and dotted lines identify input (model) and numerically calculated velocities, respectively.

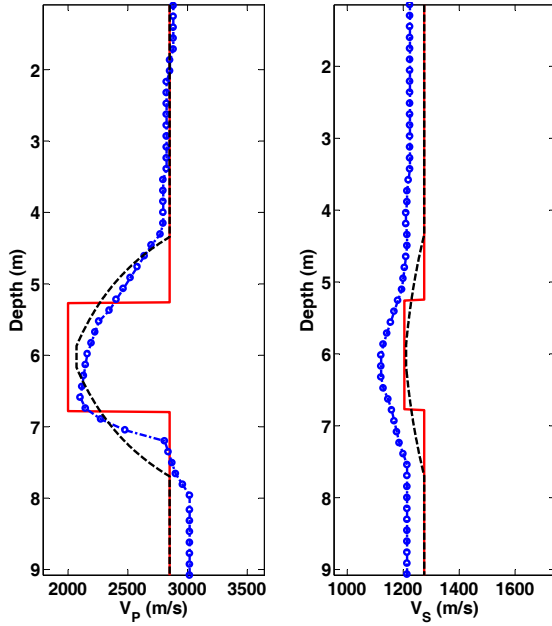


**Fig. 14:** Logs of  $V_P$  (monopole source) and  $V_S$  (dipole source) for Model 2a. Continuous and dotted lines identify input (model) and numerically calculated velocities, respectively. Fine black line identifies the theoretical averaged velocity.

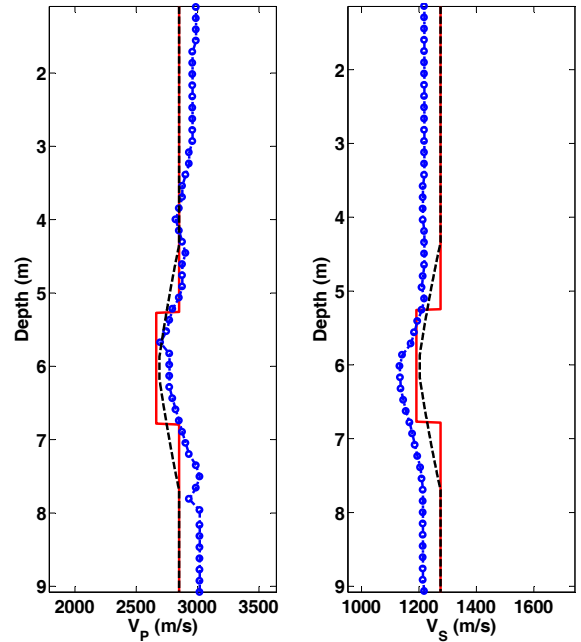


**Fig. 15:** Logs of  $V_P$  (monopole source) and  $V_S$  (dipole source) for Model 2b. Continuous and dotted lines identify input (model) and numerically calculated velocities, respectively. Fine black line identifies the theoretical averaged velocity.

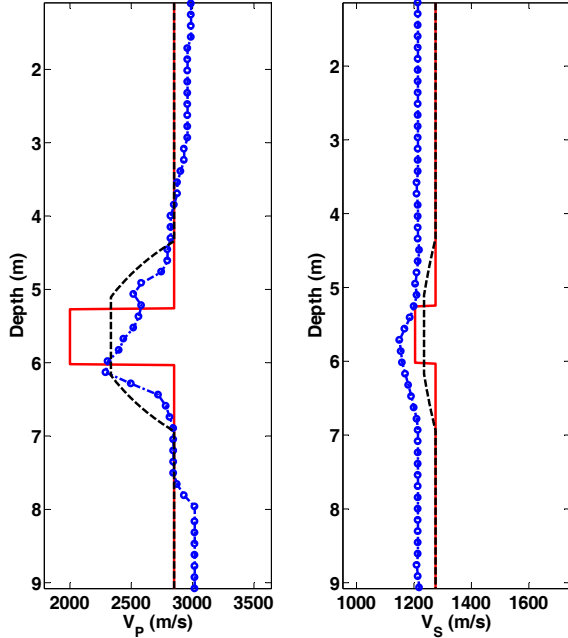


**Fig. 16:** Logs of  $V_P$  (monopole source) and  $V_S$  (dipole source) for Model 2c. Continuous and dotted lines identify input (model) and numerically calculated velocities, respectively. Fine black line identifies the theoretical averaged velocity.

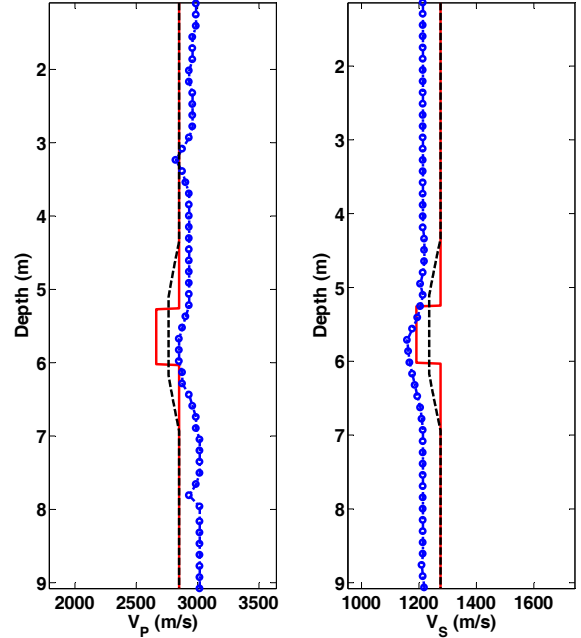


**Fig. 17:** Logs of  $V_P$  (monopole source) and  $V_S$  (dipole source) for Model 2d. Continuous and dotted lines identify input (model) and numerically calculated velocities, respectively. Fine black line identifies the theoretical averaged velocity.

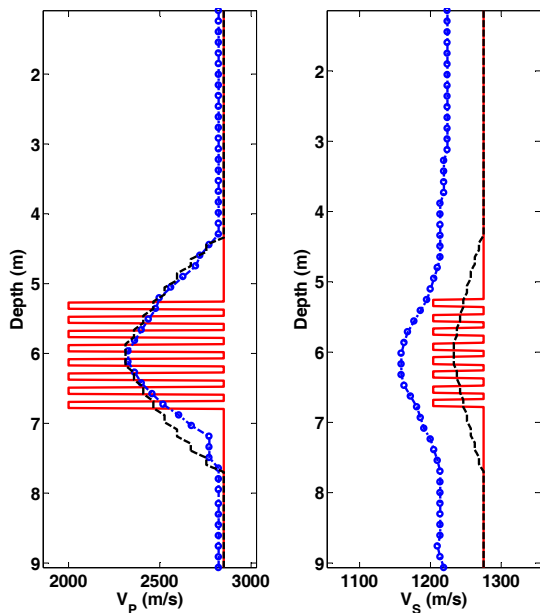


**Fig. 18:** Logs of  $V_P$  (monopole source) and  $V_S$  (dipole source) for Model 3a. Continuous and dotted lines identify input (model) and numerically calculated velocities, respectively. Fine black line identifies the theoretical averaged velocity.

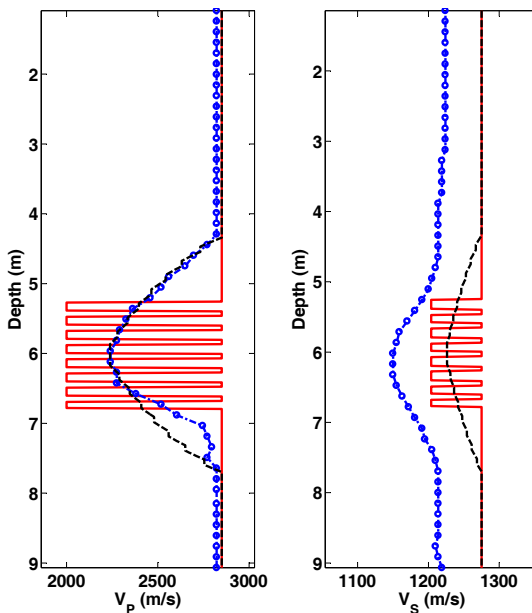


**Fig. 19:** Logs of  $V_P$  (monopole source) and  $V_S$  (dipole source) for Model 3b. Continuous and dotted lines identify input (model) and numerically calculated velocities, respectively. Fine black line identifies the theoretical averaged velocity.

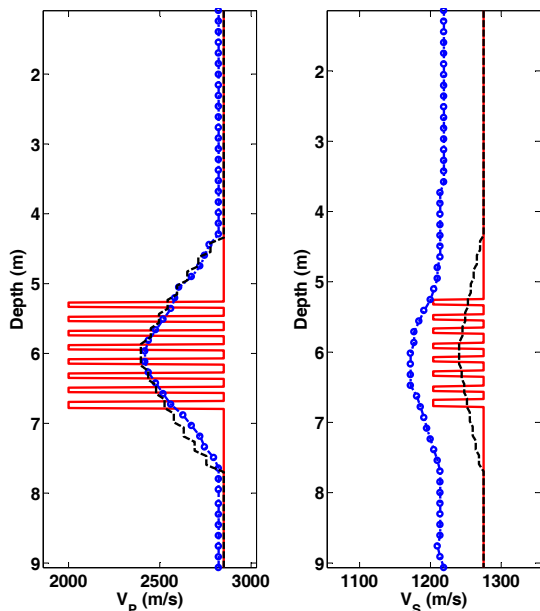


**Fig. 20:** Logs of  $V_P$  (monopole source) and  $V_S$  (dipole source) for Model 3c. Continuous and dotted lines identify input (model) and numerically calculated velocities, respectively. Fine black line identifies the theoretical averaged velocity.

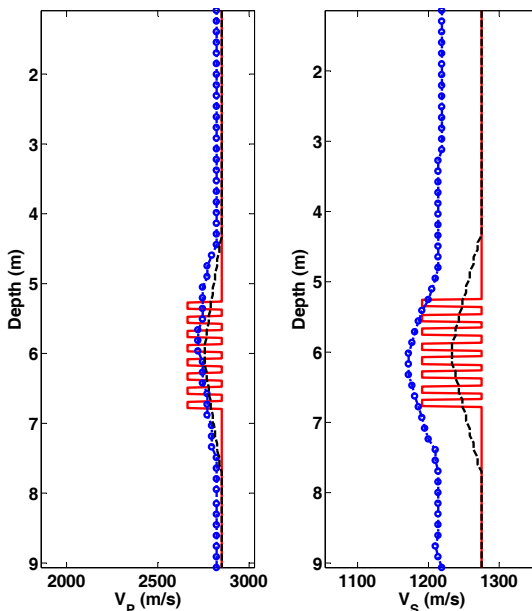


**Fig. 21:** Logs of  $V_P$  (monopole source) and  $V_S$  (dipole source) for Model 3d. Continuous and dotted lines identify input (model) and numerically calculated velocities, respectively. Fine black line identifies the theoretical averaged velocity.

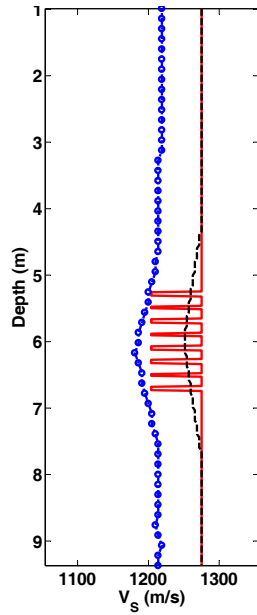
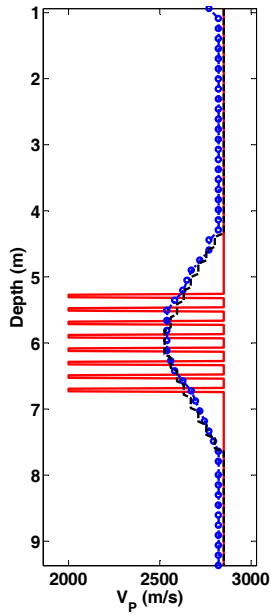


**Fig. 22:** Logs of  $V_P$  (monopole source) and  $V_S$  (dipole source) for Model 3e. Continuous and dotted lines identify input (model) and numerically calculated velocities, respectively. Fine black line identifies the theoretical averaged velocity

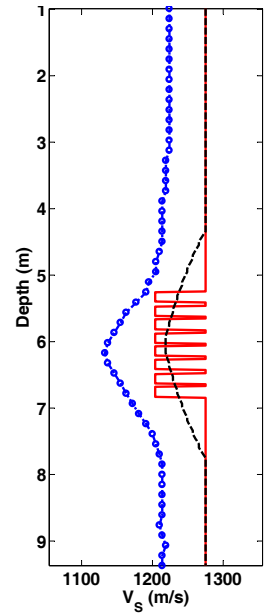
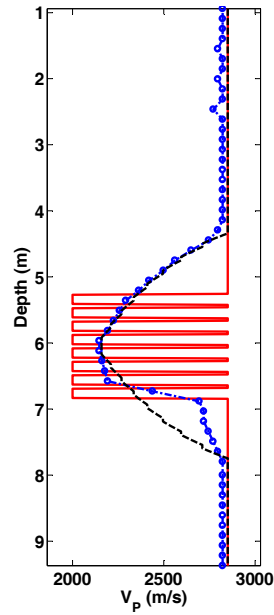


**Fig. 23:** Logs of  $V_P$  (monopole source) and  $V_S$  (dipole source) for Model 3f. Continuous and dotted lines identify input (model) and numerically calculated velocities, respectively. Fine black line identifies the theoretical averaged velocity

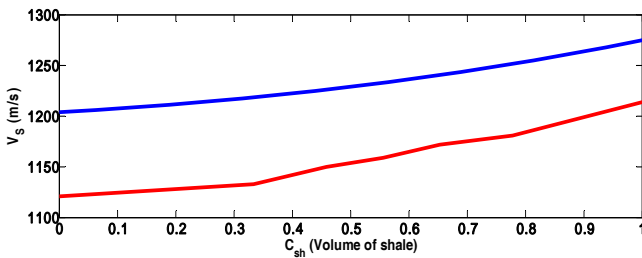
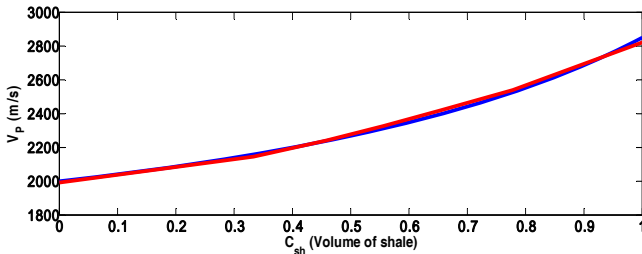


**Fig. 24:**  $V_P$  (monopole source) and  $V_S$  (dipole source) as functions of the volume of shale  $C_{SH}$  for the case of Model 3. Blue and red lines identify theoretical averages and numerically calculated velocities, respectively.

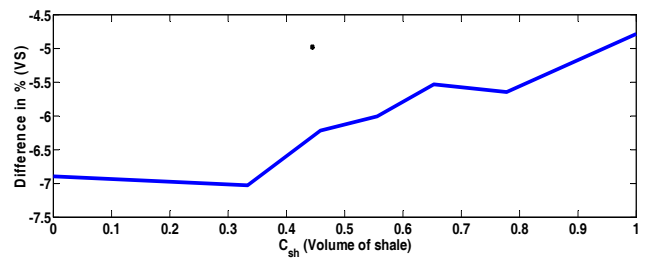
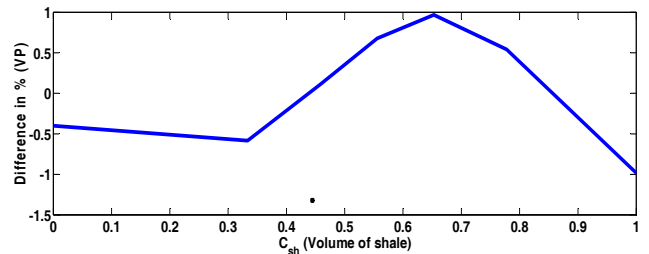


**Fig. 25:** Percentage difference in  $V_P$  (monopole source) and in  $V_S$  (dipole source) between the theoretical and the numerically calculated velocities, as functions of the volume of shale  $C_{SH}$  for the case of Model 3.

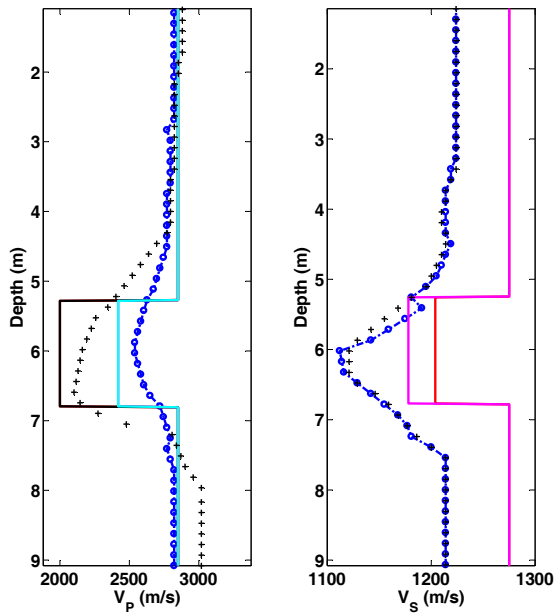


**Fig. 26:** Logs of  $V_p$  (monopole source) and  $V_s$  (dipole source) for Model 4a Continuous and dotted lines identify input (model) and numerically calculated velocities, respectively. Black crosses identify the numerical result of Model 2a.

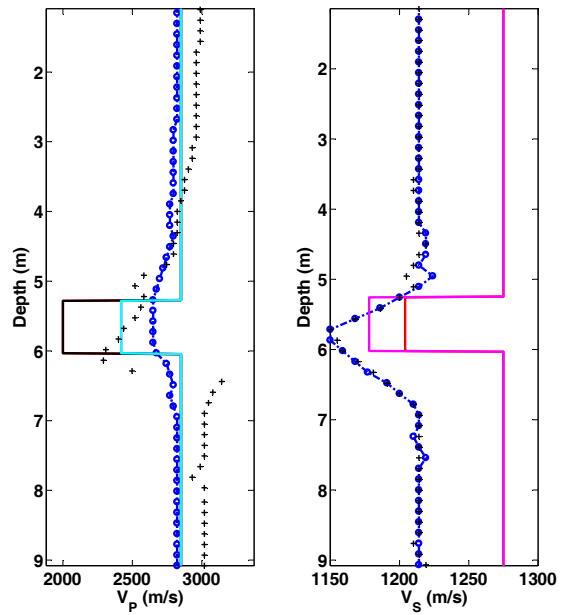


**Fig. 27:** Logs of  $V_p$  (monopole source) and  $V_s$  (dipole source) for Model 4b Continuous and dotted lines identify input (model) and numerically calculated velocities, respectively. Black crosses identify the numerical result of Model 2c.